Iron binding in the ferroxidase site of human mitochondrial ferritin

Silvia Ciambellotti,[a,b,c] Alessandro Pratesi,[d] Giusy Tassone,[e] Paola Turano,[a,b,c] Stefano Mangani,[b,c,e] Cecilia Pozzi*[e]

[a] Dr S. Ciambellotti, Prof P. Turano
Department of Chemistry "Ugo Schiff"– Department of Excellence 2018-2020
University of Florence
via della Lastruccia 2, 50019 Sesto Fiorentino (FI), Italy
[b] Dr S. Ciambellotti, Prof P. Turano, Prof S. Mangani
Magnetic Resonance Center (CERM)
University of Florence
Luigi Sacconi 6, 50019 Sesto Fiorentino (FI), Italy
[c] Dr S. Ciambellotti, Prof P. Turano, Prof S. Mangani
Consorzio Interuniversitario Risonanze Magnetiche di Metallo Proteine (C.I.R.M.M.P.)
via Luigi Sacconi 6, 50019 Sesto Fiorentino (FI), Italy
[d] Dr A. Pratesi
Department of Chemistry and Industrial Chemistry
University of Pisa
Via Giuseppe Moruzzi 13, 56124 Pisa, Italy
[e] Dr G. Tassone, Prof S. Mangani, Prof C. Pozzi
Department of Biotechnology, Chemistry and Pharmacy – Department of Excellence 2018-2020
University of Siena
via Aldo Moro, 2 53110 Siena, Italy
E-mail:cecilia.pozzi@unisi.it

Supporting information for this article is given via a link at the end of the document.

Abstract: Ferritins are nanocage proteins that store iron ions in their central cavity as hydrated ferric oxide biominerals. In mammals, further the L (light) and H (heavy) chains constituting cytoplasmic maxi-ferritins, an additional type of ferritin has been identified, the mitochondrial ferritin (MTF). Human MTF (hMTF) is a functional homopolymeric H-like ferritin performing the ferroxidase activity in its ferroxidase site (FS), in which Fe(II) is oxidized to Fe(III) in the presence of dioxygen. To better investigate its ferroxidase properties, here we performed time-lapse X-ray crystallography analysis of hMTF, providing structural evidence of how iron ions interact with hMTF and of their binding to the FS. Transient iron binding sites, populating the pathway along the cage from the iron entry channel to the catalytic center, were also identified. Furthermore, our kinetic data at variable iron loads indicate that the catalytic iron oxidation reaction occurs via a diferric peroxo intermediate followed by the formation of ferric-oxo species, with significant differences with respect to human H-type ferritin.

Introduction

Ferritins are nanocage proteins that sequester iron ions and keep them in a non-toxic and bioavailable form; indeed iron is sized and concentrated within their central cavity in the form of hydrated ferric oxide biominerals.[1] Ferritins further contribute to iron homeostasis, acting as antioxidants by storing iron coming from the cytosolic "labile iron pool", thus preventing the occurrence of Fenton-like chemistry.[2] Maxi-ferritins are characterized by a quaternary structure generated by 24 protein subunits self-assembling in hollow spherical shells, having an outer diameter of approximately 120 Å and an internal cavity ~ 80 Å across. Homopolymeric ferritin shells are highly symmetrical, with three four-fold, four three-fold, and six two-fold symmetry axes that result in a peculiar 432-point symmetry. In mammals, cytoplasmic maxi-ferritins are usually hetero-oligomers constituted by two different types of chains, classified according to their molecular weight in L (light) and H (heavy).[1,3] On the functional standpoint, the two types of chains are also distinct. H chains are deputed to ferroxidase activity, in which Fe^{2+} is oxidized to Fe^{3+} in the presence of dioxygen inside the ferroxidase site (FS; also named oxidoreductase site).[1,4] On the other hand, L-type chains are involved in iron biomineralization facilitated through a nucleation site, located on the internal cage surface, in which iron ions assemble as oxo-centered trinuclear iron(III) clusters.[1,5,6] In humans and other mammals, a further type of ferritin has been identified, namely the mitochondrial ferritin (MTF). Human MTF (hMTF), encoded by an intronless gene, is expressed as a precursor protein having a N-terminal signal peptide sequence which mediates mitochondria localization.[7] The mature protein, resulting from the signal peptide cleavage, is further processed into a functional homopolymeric ferritin able to incorporate iron.[8] Kinetic analysis performed on recombinant hMTF (including residues from 61 to 242) have shown a rate of iron oxidation remarkably slower (more than 50 %) than that displayed by the recombinant homopolymeric human H-ferritin (HuHf).[9] The authors have indicated the Ala to Ser substitution in position 144 as the major contribution to the slower reaction rate in hMTF (the standard sequence numbering, corresponding to that of HuHf is used throughout). To probe the role of this residue, the S144A variant of hMTF has been generated and investigated showing that, despite its ferroxidase activity was twice as fast than that of wild type hMTF, it remained considerably slower (~ 67 %) than HuHf.[9] This evidence strongly suggests that the different ferroxidase kinetic is not attributable only to a one-residue change in the FS but more reasonably to major changes not only localized in this site.

To better investigate the ferroxidase properties of hMTF, here we performed time-lapse X-ray crystallography analysis of hMTF to

characterize the iron binding events occurring in this ferritin. A series of medium-high resolution, anomalous diffraction experiments was performed on single protein crystals of hMTF exposed to ferrous ions for various periods of time under aerobic and anaerobic conditions. These results provided the first structural evidence of how iron ions interact with hMTF and allowed the analysis of their binding to the FS. Furthermore, detailed information on the identity of the transient iron binding sites populating the pathway along the cage from the iron entry channel to the catalytic center was obtained. This structural information was then compared to that previously reported on other vertebrate ferritins.[4,10] Kinetics measurements of the iron(II) oxidation reaction in solution were also performed and the results compared to those of HuHf.

Results and Discussion

Multiple sequence alignment. A Clustal Omega multiple sequence alignment was performed on protein sequences of hMTF and of the cytosolic HuHf and HuLf. The coding sequence of hMTF includes the amino acids 61-242, while the N-terminal 60 residues constitute the mitochondrial targeting signal. hMTF is an H-like ferritin with ferroxidase activity. Indeed, the sequence alignment with HuHf evidences an 80 % sequence identity and the complete conservation of the residues composing the ferroxidase center (Figure 1).

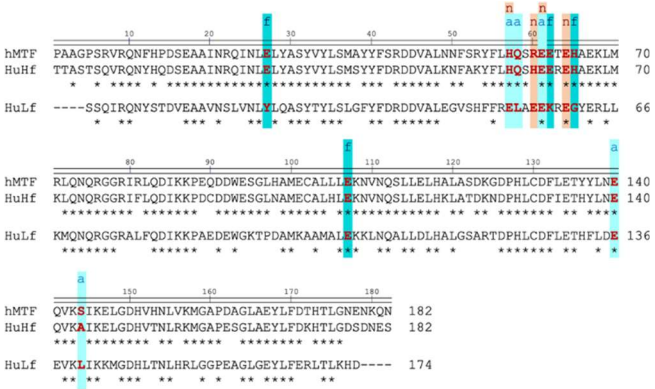

Figure 1. Sequence alignment among human mitochondrial ferritin (hMTF, UniProtKB Q8N4E7), human H ferritin (HuHf, UniProtKB P02794) and human L ferritin (HuLf, UniProtKB P02792). Conserved residues are indicated by a star (placed below the residue). The hMTF sequence used for the present study includes residues 61-242, corresponding to the HuHf residues 1-183 (the residue numbering of HuHf is used as standard sequence numbering for all human ferritins). Residues belonging to the ferroxidase site (f letter above residues) and accessory transient sites (a letter) in H type ferritins and those of the nucleation site (n letter) in L ferritins, are reported in bold red characters and highlighted light blue and orange, respectively. The N-terminal sequence mediating mitochondrial targeting and the signal peptide of hMTF (first 60 residues) are omitted from this figure. The extent of sequence identity between hMTF and HuHf is 80 % whereas only 55 % is shared between hMTF and HuLf.

Furthermore, almost the same pattern of ligands previously defined as the accessory transient iron binding sites is maintained (His57, Gln58, Glu61 and Glu140 are conserved, while hMTF Ser144 replaces Ala144 in HuHf, Figure 1). The above-mentioned residues guide incoming iron(II) ions towards the FS.[4] On the contrary, a lower extent of sequence identity (55 %) characterizes the alignment with HuLf (Figure 1). The residues identified in HuHf and HuLf as second coordination sphere ligands to the ferrous hexa-aqua ions transiting through the channels at the three-fold symmetry axes (C3), i.e. Asp131 and Glu134, are maintained in all the three ferritins (Figure 1). Also His173, which is located at the four-fold symmetry axes (C4) and traps metal ions in HuHf, is conserved in hMTF; instead, HuLf has a non-coordinating leucine (Leu169) in the same position (Figure 1).

Protein characterization in solution. From the expression in *E. coli*, about 60 mg of hMTF per liter of culture were obtained in rich medium. At the end of the purification process, the size exclusion elution chromatogram confirmed the 24mer conformation of the protein (Figure S1). After demineralization, the protein was subjected to ESI-MS analysis to confirm the expected molar mass based on its primary sequence. The theoretical molar mass of the mature hMTF subunit is 21079.395 Da, as calculated with Bio Tool Kit. Nevertheless, the deconvoluted mass spectrum (Figures S2-S6) exhibits the main signal at 20947.488 Da, corresponding to the hMTF polypeptide without the first N-terminal amino acid residue (Met, 131 Da). The other peaks at 20963.483, 20978.470 and 20994.455 Da, which differ by about 16 Da one to each other and from the main signal, can be reasonably attributed to the progressive oxidation of methionines.[11] Different samples show different concentrations of oxidized forms.

The ferroxidase activity of hMTF was evaluated in solution with a stopped-flow spectrophotometer by adding to a 100 μM solution of the protein (concentration expressed in subunits) increasing amounts of Fe^{2+} ions (from 1 to 16 ions per subunit, as in Figures S7 and S8). The formation of the transient intermediate diferric peroxo species, DFP, with a characteristic absorbance at 650 nm, and the formation of diferric oxo/hydroxo species, DFO(H), with a maximum absorbance at 350 nm, were recorded and compared to the same processes in HuHf (Figures 2A-D).

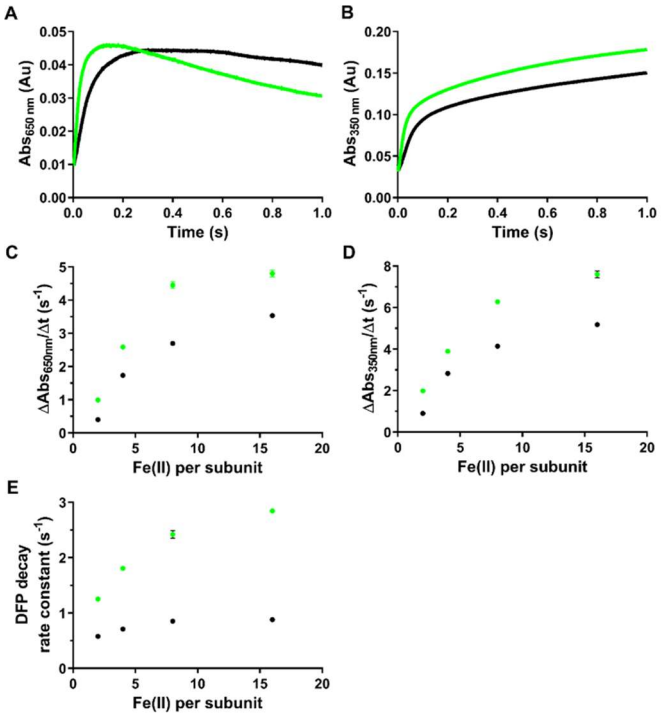

Figure 2. Iron oxidation activity measurements in hMTF (green traces) and HuHf (black traces). Single turnover oxidoreductase kinetics (2 Fe^{2+}/subunit) were monitored: DFP formation is reported as the change in absorbance at 650 nm (A panel) and DFO(H) species formation as the change in absorbance at 350 nm (B panel). The absorbance changes are zoomed in the first second to highlight the differences in the initial part of the reaction. All the curves report the mean of three replicates with SEM (standard error of the mean; indicated by the thickness of the continuous lines). In panels C and E, the dots represent the

initial rates of the DFP formation and decay, respectively, as a function of loaded iron per subunit in the two proteins (same color scheme); panel D shows the trend of initial rates of DFO(H) formation. All the data points represent the mean of three replicates with its standard deviation (not appreciable because SD values are too small).

Faster initial rates of formation and decay of the transient DFP species are observed for hMTF with respect to HuHf for different Fe^{2+}/subunit ratios (Figures 2A,C,E, S7 and S8). The effect increases by increasing the number of added iron ions (Figures 2C,E). A different turnover efficiency is revealed also from the assessment of the initial rates related to the formation of the ferric products measured at 350 nm (Figure 2D). However, the curves at 350 nm show a more complex behavior when recorded for Fe^{2+}/subunit ratios ≥4. Under these circumstances, the reaction rate for hMTF slows down as the reaction proceeds, and becomes slower than that of HuHf, with a crossing point between the corresponding curves around 1 s (Figure S8). The phenomenon is particularly evident in the curve recorded for 16 Fe^{2+} per subunit (Figure 3). The curves embed a multiphasic behavior, which comprises both the ferroxidase catalytic oxidation and the biomineralization reaction. Apparently, the former is faster in hMTF while the latter is faster in HuHf. The curves recorded over 1000 s show the same amount of final products at plateau.

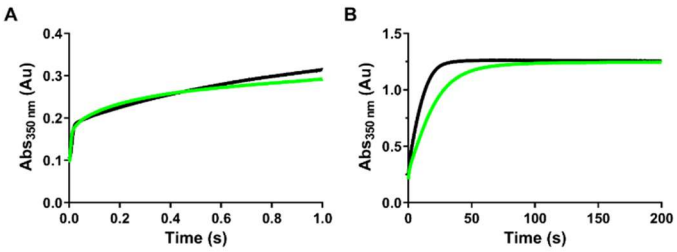

Figure 3. Ferric products formation over time. Absorbance changes at 350 nm registered over one second (A panel) and over 200 s (B panel) after the addition of 16 Fe^{2+} ions per subunit. Black curves refer to HuHf and green curves to hMTF. All the curves report the mean of three replicates with SEM.

Time-lapse crystallographic studies of hMTF. A series of structures of hMTF were obtained through an established protocol, relying on time-lapse crystallography,[4,10,12,13] which allows us to describe the evolution of the iron binding events with time. Crystals of iron-free hMTF were exposed to Fe^{2+} (by adding saturated Mohr's salt solution in the crystallization drop to provide a large excess of the substrate metal ion) under aerobic conditions and frozen after 1, 3, 5, 15, 60, 90, and 120 minutes of free iron diffusion. A second series of structures was obtained on crystals grown under anaerobic conditions and loaded with Fe^{2+} for 3, 5 and 15 minutes. In this case, the diffusion time of 15 minutes was the maximum possible before crystal cracking that prevented further characterization.

The structure of the iron-free hMTF (see SI-S1 and Figure 4A) was obtained as the reference structure. Comparison with the previously reported model (PDB id 1R03)[9] does not show significant differences and magnesium ions (from the crystallization environment) populate the FS (Figure S9B). In all the structures determined, the visible hMTF chain starts at residue Gly4 or Pro5 and ends at residue Gly176. The tertiary structure of hMTF, shared among all ferritins,[1] consists of a bundle of four helices (α1-α4) with a fifth short C-terminal helix (α5) tilted by ~ 60° on the long axis of the bundle (Figure 5). Shared is also the typical maxi-ferritin quaternary structure, generated by the self-assembly of 24 subunits to form hollow cages. The asymmetric unit of hMTF crystals includes a single protein chain, representing the spatial and time average of all protein subunits, as reported previously.[4–6,10] Depending on the iron-diffusion time, the structures of hMTF include a variable number of metal ions [Mg(II) and/or Fe(II)/(III) ions] whose chemical nature was discriminated according to the detected anomalous diffraction signal. Iron ions are characterized by a strong signal in the anomalous difference Fourier map determined from data collected with X-ray energy of ~7130 eV (Fe K-edge peak) that disappeared in the map computed from the data collected at energy immediately below this edge. The determination of the oxidation state of each iron ion is more ambiguous and was inferred by the comparison with

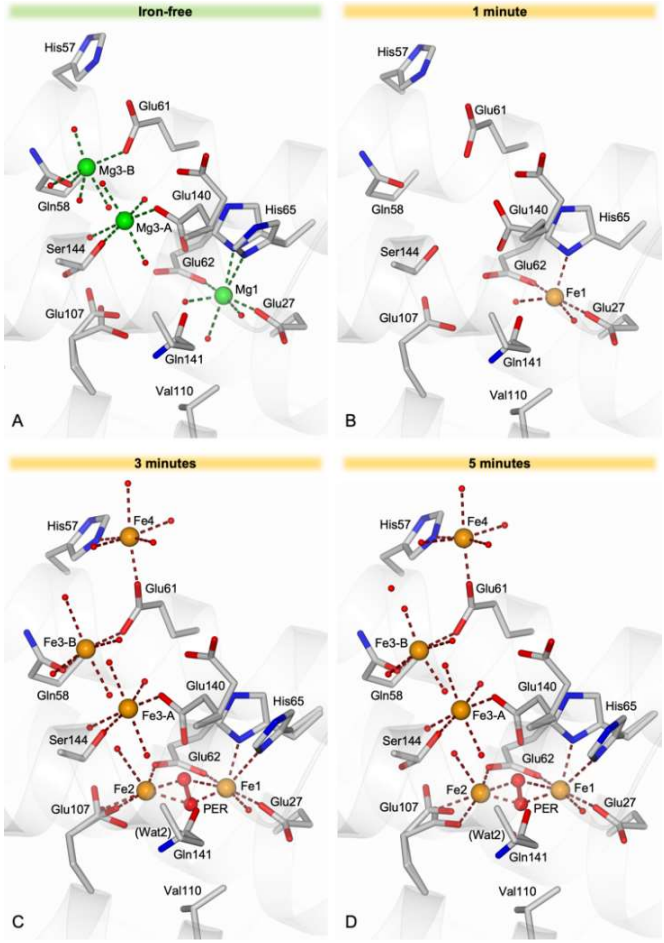

previous structural and spectroscopic studies performed on ferritin enzymes and model compounds (*vide infra*).

Figure 4. FS view of hMTF (light grey cartoon and carbon atoms) in the iron-free state (A panel) and after 1 (B), 3 (C) and 5 (D) minutes of free iron diffusion. Coordination bonds for magnesium and iron ions (green and orange spheres, respectively, of arbitrary radius) are displayed as dark green and dark red dashed lines. After 1 min of iron exposure (B panel) the metal binding site 1 is populated by iron ions (Fe1). In the structures determined after 3-5 min of free iron diffusion (C and D panels) Fe1 and Fe2 are bridged by a peroxide species (PER, displayed as red ball-and-stick model). Furthermore, in these structures other Fe ions occupy two alternate positions: Fe3-A, is anchored to Ser144 (A-conf) and Glu140 (A-conf), whereas Fe3-B is coordinated by Gln58 and Glu61. Fe3-A and Fe3–B are in positions analogous to those observed for Mg-A and Mg–B (A panel). In all figures, water molecules are displayed as red spheres (arbitrary radius); nitrogen and oxygen atoms are colored blue and red, respectively.

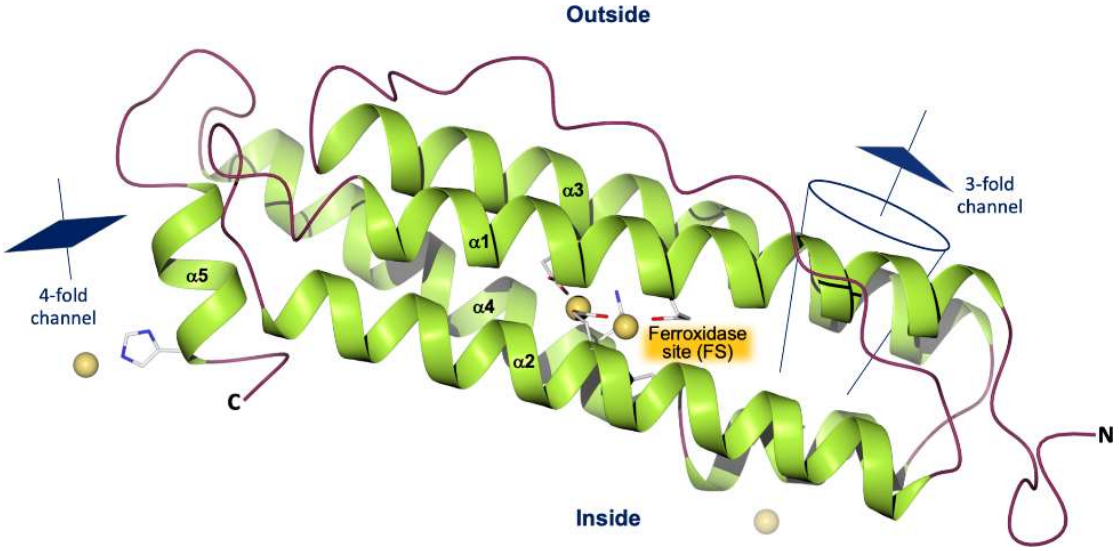

Figure 5. hMTF subunit represented as light-green ribbon (the five α-helices are sequentially numbered from the N-terminus). The FS is highlighted by the presence of iron ions (pale orange spheres, arbitrary radius), coordinated to FS-residues (in sticks, white carbons). Three-fold and four-fold channel locations are indicated (iron ions and amino acid residues inside the channels are displayed).

No meaningful changes are observed in the protein fold upon exposure to iron ions. Crystallographic determinations provide average molecular structures and, especially at atomic resolution, the spatial disorder is evident. The disorder appears more relevant when chemical events are occurring in the crystal, as it happens in ferritins when dioxygen and iron are diffusing into crystals and are trapped after short substrate exposure times. In this case, alternate conformations of side chains and positions of solvent or exogenous molecules (e.g. dioxygen) cannot be fully described.

In the crystal structures presented in this work, we have limited the interpretation of the electron density to the strongest peaks present in the Difference and Anomalous Difference Fourier maps. After refinement, unexplained electron density remains in the FS site. The disorder is indicative of a mixture of binding events occurring in different unit cells of the crystal related to the processing of iron ions. The detailed descriptions of all crystal structures are reported in SI. Here, we only describe the coordination environment of iron ions and how the number of metal ions and their coordination spheres change with time.

Metal binding sites in FS. Figures 4A-D show magnesium binding to FS (A) compared with iron at 1 (B), 3 (C), 5 (D) minutes of exposure to Mohr's salt. After 1 minute, the anomalous difference map shows only the iron binding site 1 occupied by iron ions (Fe1, most probably as Fe^{2+}, refining at 50% occupancy; Figures 4B and 6A and Table S1). Fe1 is coordinated in a square pyramidal geometry by Glu27, Glu62 (as monodentate ligands) and two water molecules at the base and by His65 Nδ1 at the vertex. Such coordination is conserved in all vertebrate catalytic maxiferritins studied so far.[4,10] The proximal Val110 (4.23 Å from Fe1) prevents completion of octahedral geometry.[4,10] Figures 4C,D and 6B,C show how the population of the FS by iron ions evolves with soaking time. At 3 minutes, the catalytic site is completed by the second iron ion (Fe2) bound to the iron site 2, consisting of Glu107 (bidentate) and Glu62 that bridges it to Fe1 of the dinuclear cluster. The occupancy is estimated to 85 % and 50 % for Fe1 and Fe2, respectively (SI-S2 and Table S1).

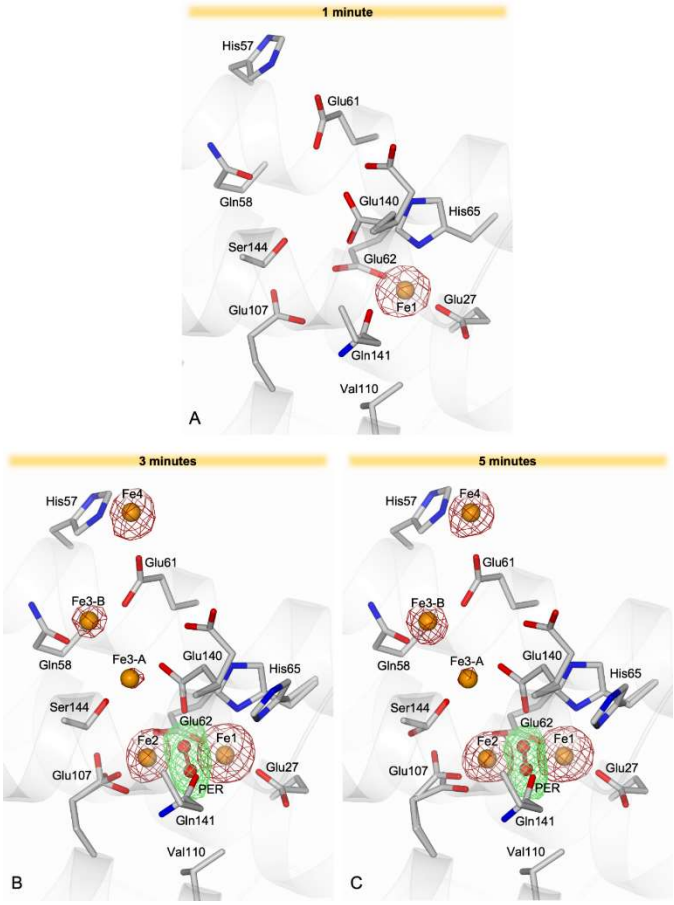

Figure 6. Ferroxidase site view of hMTF (light grey cartoon and carbon atoms) after A) 1, B) 3, and C) 5 minutes of free iron diffusion. Iron ions (orange spheres of arbitrary radius) are surrounded by the anomalous difference map (dark-red mesh) contoured at 4.0 σ. In the structures determined after 3 and 5 minutes of free-iron diffusion (B and C panel, respectively) Fe1 and Fe2 are connected by a peroxide species (PER, displayed as red ball-and-stick model), surrounded by the omit map (green mesh) contoured at 3.0 σ.

In both structures an elongated, significant, residual electron density is observed in between Fe1 and Fe2 (Figures 6B,C). The shape and size of this density suggest the presence of a diatomic species bridging the two iron ions in a Fe-Fe μ-η^2:η^2 side-on coordination. The refinement (see SI) supports the presence of a peroxide anion (interatomic O-O distance of 1.40 Å). The same coordination of Fe1 and Fe2 is observed in the 5-minute structure. Three additional iron ions bound in the FS cavity (Figures 4C,D) are observed in the anomalous difference maps of the two structures (Figures 6B,C). Each iron ion is bound only to two amino-acid side chains and completes an almost regular octahedral coordination geometry by binding water molecules. Two of these iron ions, named Fe3-A and Fe3-B, have been interpreted as mutually exclusive since their positions are too close (3.2 Å) to be simultaneous without bridging ligands. Fe3-A and Fe3-B replace the Mg(II) ions observed in matching sites of the iron-free structure (Figure 4A). Fe3-A and Fe3-B show 20 % and 40 % occupancy, respectively, while Fe4 refines to 40 % occupancy (Table S1). Taken together their positions suggest a possible pathway of iron ions moving from the inner cage surface towards the catalytic site. When the exposure time raises to 15 min, the configuration of the FS undergoes further interesting changes. Both the Fe1 and Fe2 sites of the FS are still populated by iron ions (occupancies estimated to 85 and 60 %, respectively, TableS1), now bridged by a water/hydroxide species (Table 1).

In the Fe2 coordination sphere a new species appears (Figures 7A and 8A), interpreted either as a dioxygen or as a superoxide anion η^2 side-on bound to Fe2 (attempts to fit the electron density with peroxide gave an unrealistic model). Fe2 distances of 2.38 (± 0.15) Å are observed from both oxygen atoms (OXY O1 and O2, Table 1). The Fe2 site structure might show either a Fe^{2+}-dioxygen adduct or a Fe^{3+}-superoxide complex. We ruled out the possibility of two water molecules in alternate positions because of the continuous electron density and since this would result in a highly distorted iron coordination geometry. The coordination of the biatomic molecule to Fe2 observed from 15 minutes onwards is very similar to that reported for the extensively characterized $[Fe^{III}(TAML)(O_2)]^{2-}$ Fe^{3+}-superoxo complex and the comparison favors this latter model.[14]

The intermetallic distance Fe1-Fe2 is now 3.36 (± 0.15) Å (Tables 1), consistent also with a mixed-valence Fe^{2+}-Fe^{3+} cluster.[15,16] The above-described coordination of Fe1 and Fe2 sites is maintained up to the maximum time achievable (120 minutes; Figures 7A-D and 8A-D; Tables 1 and S1).

	Fe^{2+} 3' (± 0.08 Å)		Fe^{2+} 5' (± 0.06 Å)			Fe^{2+} 15' (± 0.15 Å)		Fe^{2+} 60' (± 0.10 Å)		Fe^{2+} 90' (±0.11 Å)		Fe^{2+} 120' (± 0.11 Å)	
	Fe1	**Fe2**	**Fe1**	**Fe2**		**Fe1**	**Fe2**	**Fe1**	**Fe2**	**Fe1**	**Fe2**	**Fe1**	**Fe2**
Fe2	**3.45**	-	**3.42**	-	**Fe2**	**3.36**	**-**	**3.41**	**-**	**3.42**	**-**	**3.40**	**-**
His65-A Nδ1 His65-B Nδ1	2.14 2.49		2.20 2.33		His65 Nδ1	2.20		2.24		2.22		2.27	
Glu27 Oε2	2.00		2.03		Glu27 Oε2	2.00		2.04		2.05		2.09	
Glu62 Oε1	2.06		2.02		Glu62 Oε1	2.04		2.07		2.11		2.13	
Wat1	2.16		2.15		Wat1	2.33		2.14		2.23		2.21	
PER O2	2.42	1.97	2.47	2.01	Wb	2.06	1.87	2.13	1.82	1.96	1.85	2.07	1.87
PER O1	1.78	1.97	1.86	1.77	OXY O1	2.58	2.38	2.77	2.41	2.75	2.35	2.75	2.37
Wat2	2.76	2.43	2.76	2.38	OXY O2		2.38		2.40		2.46		2.36
Glu62 Oε1		1.99		2.00	Glu62 Oε1		1.97		1.95		2.01		1.97
Glu107-A Oε1 Glu107-B Oε1		2.13 2.04		2.01 2.20	Glu107 Oε1		2.12		2.18		2.20		2.18
Glu107-A Oε2 Glu107-B Oε2		2.11 2.21		2.15 2.33	Glu107 Oε2		2.33		2.11		2.10		2.07
Wat3		2.45		2.28	Wat3		2.39		2.19		2.21		2.24

Table 1. Iron coordination distances in the FS. Panels show FS views of hMTF (light grey carbons) and after 5 (left) and 15 (right) minutes of free iron diffusion (iron ions are shown as orange spheres of arbitrary radius). Coordination and H-bonds are displayed as dark red and azure dashed lines. In the structures determined after 3-5 minutes of iron exposure, a peroxide anion (PER, red ball-and-stick model) bridges the two iron ions. On the other hand, Fe1 and Fe2 are bridged by a water/hydroxide species (Wb) in the structures determined after 15-120 minutes and a dioxygen or superoxide anion (OXY, red ball-and-stick model) is side-on bound to Fe2.

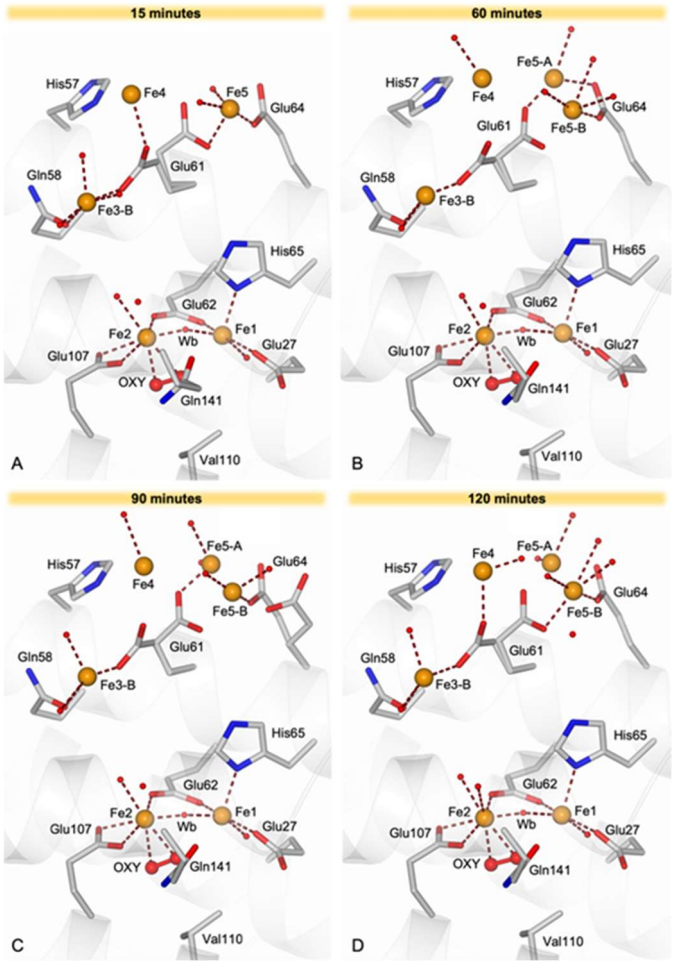

Figure 7. Ferroxidase site view of hMTF (light grey cartoon and carbon atoms) after A) 15, B) 60, C) 90, and D) 120 minutes of free iron diffusion. Coordination bonds for iron ions (orange spheres of arbitrary radius) are displayed as dark red dashed lines. In the FS of all structures, Fe1 and Fe2 are bridged by a water/hydroxo species (Wb, red sphere). Furthermore, the pose of the oxygen/superoxide molecule (OXY, shown as red ball-and-stick model) coordinating Fe2 side-on is shown. Starting from 15 min exposure an additional iron binding site: Fe5, becomes populated. Fe5 ions are anchored by Glu61 (B-conformation) and Glu64. Upon increasing the iron diffusion time, two alternate positions are observed for iron ions in this site, named Fe5-A and Fe5-B (B-D panels).

On the other hand, the population of the accessory iron binding sites beyond the FS changes with time, resulting in the presence of iron ions only in the Fe3-B and Fe4 sites (populated to 40 % and 30 %, respectively, Table S1), whereas those occupying the Fe3-A site observed after 3-5 min iron exposure are no longer visible in the structure. After 15 min iron exposure a further site, named Fe5, becomes populated to a low extent (estimated to 30 %, Table S1), in which the iron ion is anchored to two glutamate residues, namely Glu61 (B-conformation) and Glu64 (Figure 7A and 8A). The coordination sphere of the iron ion in this site, exposed on the internal protein surface, is not well defined. This structure further highlights the key role played by Glu61 whose A-conformation shuttles the Fe3 ions (Fe3-B in Figures 4C,D), whereas the B-conformation anchors Fe5 ions (Figure 7A), strongly suggesting that the concomitant population of these sites in hMTF has to be excluded. The Fe3-A sites, observed at shorter times (Figures 4C,D), are now empty.

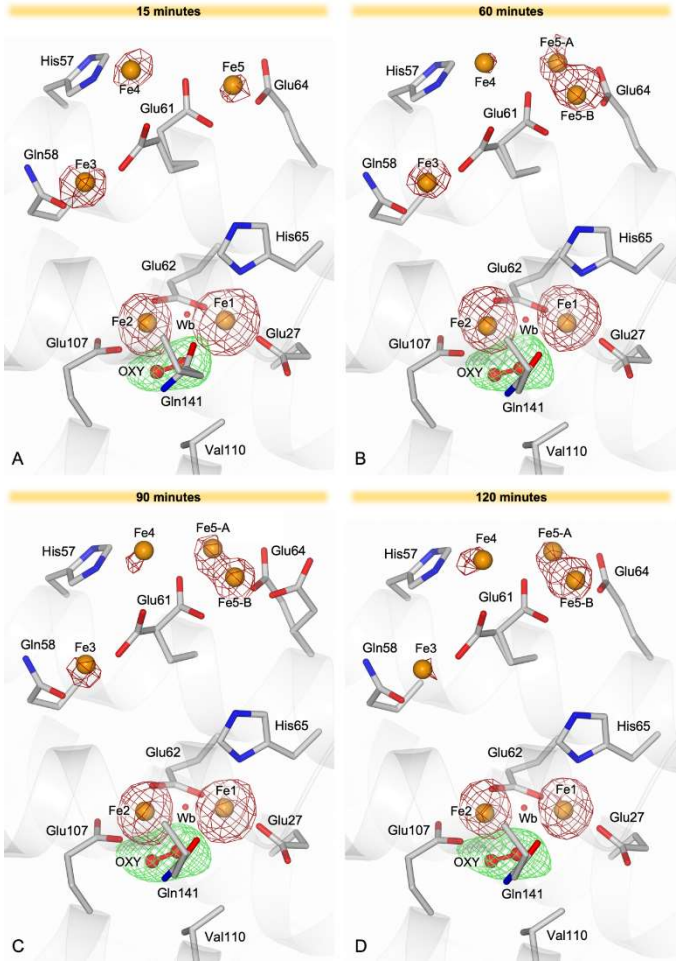

Figure 8. Ferroxidase site view of hMTF (light grey cartoon and carbon atoms) after A) 15, B) 60, C) 90, and D) 120 minutes of free iron diffusion. Iron ions (orange spheres of arbitrary radius) are surrounded by the anomalous difference map (dark-red mesh) contoured at 4.0 σ. In all structures, Fe2 is coordinated side-on by an oxygen/superoxide molecule (OXY, shown as red ball-and-stick model), surrounded by the omit map (green mesh) contoured at 3.0 σ. In the FS of all structures, Fe1 and Fe2 are bridged by a water/hydroxo species (Wb, red sphere).

On the other hand, the population of the accessory iron binding sites beyond the FS changes with time, resulting in the presence of iron ions only in the Fe3-B and Fe4 sites (populated to 40 % and 30 %, respectively, Table S1), whereas those occupying the Fe3-A site observed after 3-5 min iron exposure are no longer visible in the structure. After 15 min iron exposure a further site, named Fe5, becomes populated to a low extent (estimated to 30 %, Table S1), in which the iron ion is anchored to two glutamate residues, namely Glu61 (B-conformation) and Glu64 (Figure 6A and Figure 8A). The coordination sphere of the iron ion in this site, exposed on the internal protein surface, is not well defined. This structure further highlights the key role played by Glu61 whose A-conformation shuttles the Fe3 ions (Fe3-B in Figures 4C,D), whereas the B-conformation anchors Fe5 ions (Figure 6A), strongly suggesting that the concomitant population of these sites in hMTF has to be excluded. The Fe3-A sites, observed at shorter times (Figures 4C,D), are now empty.

Iron binding under anaerobic conditions. In order to validate our interpretation of the electron density in the catalytic site as Fe-bound dioxygen species, we determined three high-resolution structures of hMTF from crystals exposed to Fe^{2+} ions for 3, 5 and 15 minutes under strict anaerobic conditions (1.47 Å, 1.32 Å and 1.20 Å, respectively). The three structures show iron ions bound to the Fe1, Fe2, Fe3-A, Fe3-B and Fe4 sites (Figures 9A-C and 10A-C). Fe1 and Fe2 have occupancies estimated to 80-100 % and 40-65 %, respectively (Table S1), reporting an intermetallic distance of 3.42 - 3.47 Å. The Fe1 and Fe2 ions bind the same hMTF residues as in aerobic structures. However, two alternate orientations are observed for the side chain of His65, differing by a rotation on the Cα-Cβ bond of ~ 40°.

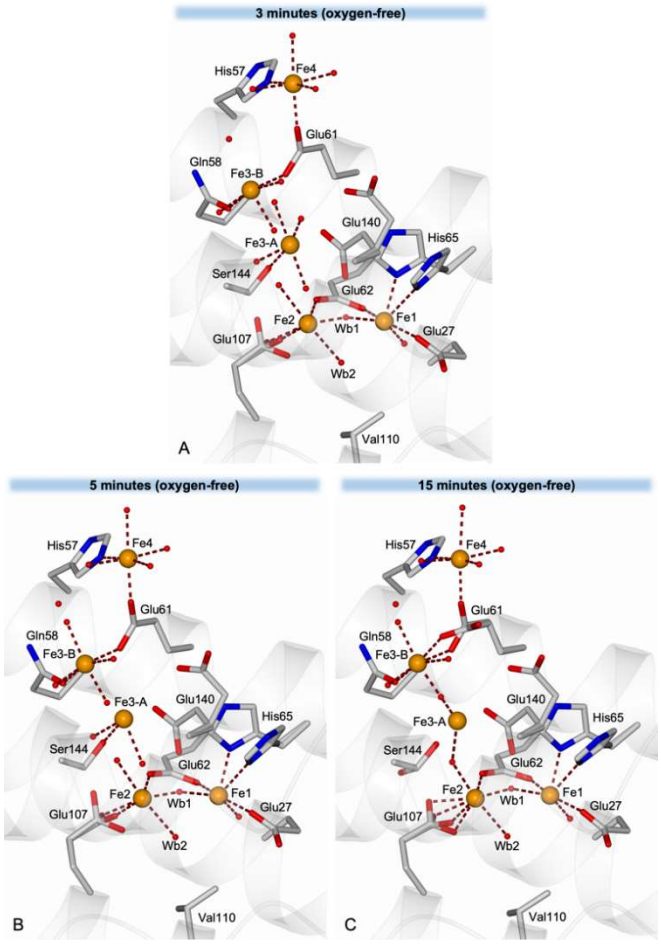

Figure 9. Ferroxidase site view of hMTF (light grey cartoon and carbon atoms) after A) 3, B) 5, and C) 15 minutes of free Fe^{2+} diffusion under strict anaerobic conditions. Coordination bonds for iron ions (orange spheres of arbitrary radius) are displayed as dark red dashed lines. Fe1 and Fe2 are connected by two water/hydroxo bridging species, Wb1 and Wb2 (red spheres). The side chain of Gln141 is omitted for clarity.

The population of the second orientation increases with time, being 20 % and 40 % after 3 and 15 minutes of Fe^{2+} exposure, respectively. The rotation of His65 within the ferroxidase site is unusual and it has never been reported for vertebrate ferritins.[4,10] The carboxylate group of Glu107, coordinating Fe2 in a bidentate fashion, is also observed in two orientations. In addition to Glu62, Fe1 and Fe2 are bridged by two water/hydroxide species, Wb1 and Wb2 (Figures 9 and 10), both positioned closer to Fe2 (Fe2-Wb1 1.90 ± 0.04 Å, Fe1-Wb1 2.28 ± 0.04 Å, Fe2-Wb2 2.41 ± 0.04 Å, Fe1-Wb2 2.69 ± 0.04 Å distances in the 15 min structure; the same distances, within experimental errors, are also observed in the 3 and 5-min structures). The comparison between the structures determined after 15 min Fe^{2+} exposure under aerobic and anaerobic conditions, shows that Wb2, present under anaerobic conditions, is replaced by the dioxygen/superoxide molecule in the aerobic environment (Wb2 matches the position of O1 of the diatomic molecule).

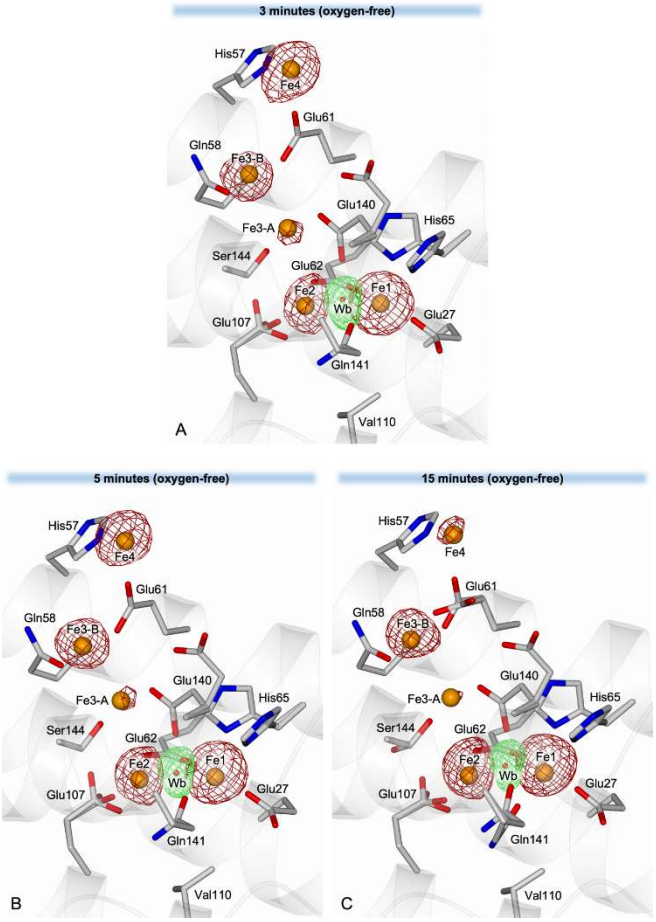

Figure 10. Ferroxidase site view of hMTF (light grey cartoon and carbon atoms) after A) 3, B) 5, and C) 15 minutes of free iron diffusion under anaerobic conditions. Iron ions (orange spheres of arbitrary radius) are surrounded by the anomalous difference map (dark-red mesh) contoured at 4.0 σ. In the FS of all structures, Fe1 and Fe2 are bridged by a water/hydroxo species (Wb, red sphere), surrounded by the omit map (green mesh) contoured at 3.0 σ.

Additional iron binding sites in 3-fold and 4-fold symmetry channels. It has been demonstrated that the 3-fold symmetry channels represent the main entrance of iron ions into the ferritin shells, while the function of 4-fold channels has still to be fully ascertained.[4,10,17–21] In the structures of iron-treated hMTF, we have observed iron binding analogous to that found in other vertebrate ferritins.[4–6,10] A detailed description of iron binding in both types of channels is given as SI (see SI-S3.1 and SI-S3.2; Figures S10 and S11; Tables S2 and S3).

Insights in the ferroxidase process of hMTF in comparison with other vertebrate ferritins. Kinetic data in solution under controlled iron loading give information on the fast events that lead to the formation of the diferric-peroxo intermediate and to the ferric-oxo/hydroxo products. On the other hand, the crystallographic time-lapse determinations provide snapshots of

the iron uptake process in conditions of free iron diffusion into the crystal. These events cannot be directly correlated with the kinetic measurements,[4,10,13] but rather with thermodynamic aspects of the process. The structures at different times provide insight into the events of iron binding to the nanocage, by showing the progressive occupancy of multiple sites by iron, from the highest to the lowest affinity sites. At variance with previous reports on hMTF,[22] our kinetic data in solution are consistent with a full set of 24 active ferroxidase centers in hMTF, that give rise to the transient formation of diferric-peroxo intermediates that then evolve into ferric oxo species on a similar time scale as observed for homopolymeric recombinant HuHf and *Rana catesbeiana* H' ferritin (*Rc*H'f). Nevertheless, significant albeit small differences are observed when comparing the reaction kinetics between the two human enzymes. At low Fe^{2+}/subunit ratios, the mitochondrial protein has faster rates of formation and decay of the transient DFP species, and the effect is more evident by increasing the metal/subunit ratio. Instead, the formation of ferric-oxo species slows down at Fe^{2+}/subunit ratios ≥4. The behavior has been reproduced on several different protein preparations and the ferritin identity has been verified by high-resolution mass spectrometry. Although different preparations have different content of oxidized methionines, the kinetic data are highly reproducible thus ruling out the role of methionines in the iron oxidation reaction. With the data in our hands, we are unable to explain the inconsistency with the previous work on hMTF.[9,22]

Our crystal structures show the population of the protein sites by iron species that develop with time, in a sort of backward path, from the most thermodynamically stable ones, after few minutes of iron exposure, to the weaker accessory transient sites. In the crystals, the latter sites become observable only at longer times, when the rate of the ferroxidation reaction decreases.

The slower turnover in the crystal also allows the observation of possible reaction intermediates. Indeed, dioxygen/superoxide and peroxide complexes have been detected following the binding of dioxygen to Fe^{2+}, as possibly captured by the structures obtained at longer exposure times. On the other hand, given the specific localization of hMTF in an environment rich in reactive oxygen species, these adducts may be consistent with a radical scavenging role for hMFT based on its ability to bind such species, as early proposed.[22] Despite the different bridging species connecting the two metal ions, the intermetallic distance Fe1-Fe2 remains quite constant, showing values ranging from 3.36 to 3.45 Å (Table 1). A similar situation has been reported for HuHf, with an intermetallic distance of 3.49 Å.[4] These distances are the same (within experimental errors) and are consistent either with a fully reduced Fe-Fe cluster or with a mixed valent complex. In mixed valent hydroxyl-bridged model compounds Fe1-Fe2 distances are in the range 3.40-3.63 Å.[23,24] The mixed-valence structure of methane monoxygenase reports a Fe^{2+}-Fe^{3+} distance of 3.4 Å.[15] Similar distances have been also observed in μ-carboxylato, μ-oxo, and μ-peroxo model compounds.[24,25] On the other hand, the distance for mixed valence Fe-Fe site found in *Synechococcus* ferritin is much longer (3.90 Å), possibly due to differences in the active site environment (e.g. the presence of a Thr in *Synechococcus* ferritin in place of Val110 in hMTF, and/or a different protonation state of the bridging water).[26]

Figure 11 shows a view of the active site of hMFT and HuHf determined after short iron exposure times (both under aerobic conditions), whereas Figure 12 highlights the comparison between the FS and accessory transient iron binding sites collectively observed in both ferritins.

By no means such comparisons should be taken as indication of the occurrence of effective mechanistic differences in the two enzymes. The structural evidences only confidently indicate that the oxidation reactions occur in both enzymes involving dioxygen species with the assistance of essentially conserved surrounding residues.

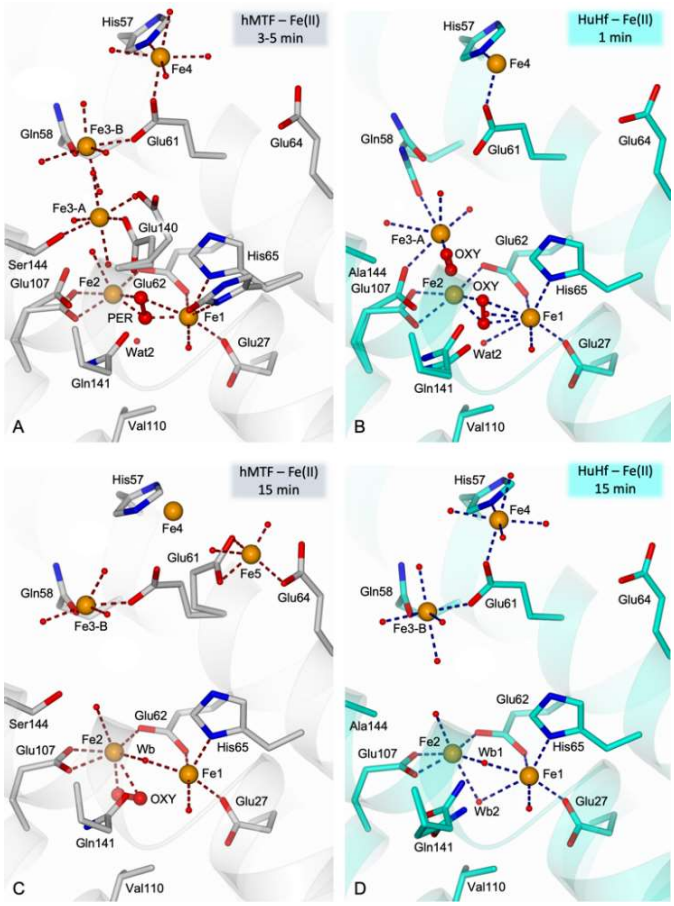

Figure 11. Ferroxidase site view of hMTF (light grey carton and carbon atoms) after 3-5 minutes (A) and 15 minutes (C) of free iron diffusion, compared with HuHf (cyan cartoon and carbon atoms) after 1 minute (B) and 15 minutes (D) exposure. Coordination bonds for iron ions (orange spheres of arbitrary radius) are displayed as dark red and dark blue dashed lines in hMTF and HuHf, respectively. Panel A shows a bi-atomic Fe1-Fe2 μ-η^2:η^2 bridging species in the FS, interpreted as a (hydrogen)-peroxide (PER, red ball-and-stick model). Panel B shows a different bridging biatomic species interpreted as a dioxygen (OXY, red ball-and-stick model). Such biatomic species is observed in hMTF at longer exposure time (panel C) in a different coordination mode. A water/hydroxo species (Wb, red sphere) bridges the iron ions in the FS of both enzymes after prolonged exposure times (C and D panels).

It can be appreciated that the distribution of iron ions is remarkably conserved, indicating similar pathways for reaching the catalytic site. Besides the Fe5 site of hMFT, the main difference is the Fe3-A site in hMTF that can be reasonably attributed to the presence of Ser144 in place of alanine in HuHf. The key role played by negatively charged glutamate and aspartate residues in this area to attract iron ions and to ensure the correct reaction turnover in the FS was previously shown in HuHf and *Rc*H'f.[12] In HuHf the replacement of Glu140 with either an alanine (E140A variant) or a glutamine (E140Q variant)

drastically reduced the enzyme kinetics.[27] Analogously, the replacement of Glu57 and Glu136 of *Rc*H'f, corresponding to Glu61 and Glu140 in hMTF and HuHf, with alanine residues (E57A-E136A double variant) impaired the enzyme catalytic function.[20] Remarkably, evidence on the *Rc*H'f variant E57A-E136A-D140A proved that these charged residues are fundamental to ensure an efficient reaction turnover without altering the ability of the enzyme to correctly bind Fe1 and Fe2 in the FS, whose presence was detected in the catalytic site of the triple variant by X-ray crystallographic analysis.[12]

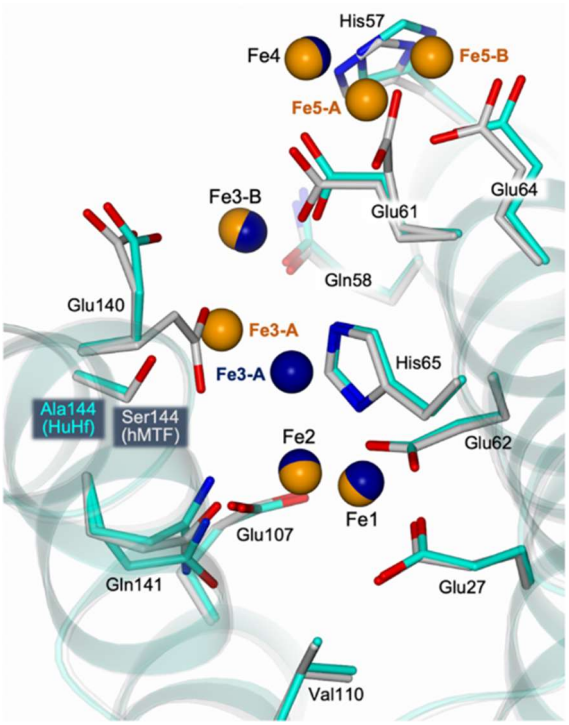

Figure 12. Superimposition between the iron binding sites observed in the ferroxidase site of hMTF (light grey cartoon and carbon atoms, iron ions displayed as orange spheres of arbitrary radius) and those previously reported in HuHf (cyan cartoon and carbon atoms, iron ions displayed as dark blue spheres of arbitrary radius) as observed at different exposure times (HuHF PDB codes: 4Y08, 4ZJK, 4OYN, 4YKH).[4] Further Fe1 and Fe2, two common sites, Fe3-B and Fe4, are shared between the enzymes. On the contrary, the positions of the Fe3-A sites (populated in HuHf only in the structure determined after 1 minute of iron exposure) are different in the two enzymes (placed ~ 2.4 Å apart). Furthermore, an additional iron binding site, named Fe5, is observed in hMTF that does not match any of the sites previously characterized in HuHf.

At diffusion times longer than 5 minutes, the Fe3-A site of hMTF disappears while the population of the Fe5, representing an additional accessory transient site, builds up. Fe5 is bound to Glu61 and Glu64 that match two of the four glutamates composing the iron mineralization site of HuLf (Glu57, Glu60, Glu61, Glu64). Glu57 and Glu60 are replaced by His57 and Arg60 in hMTF (Figure 1). Recent structural evidence, showed that three of these glutamates, namely, Glu60, Glu61 and Glu64 are responsible for anchoring oxo-centered tri-iron(III) clusters on the internal cage surface of HuLf, whereas the fourth glutamate, Glu57, is mainly involved in shuttling the incoming iron ions towards the cluster (Figure 13).[5,6] The position of the Fe5-A site observed in hMTF matches the position of one of the ferric ions (Fe2 in Figure 13) composing the trinuclear cluster in the mineralization site of HuLf.

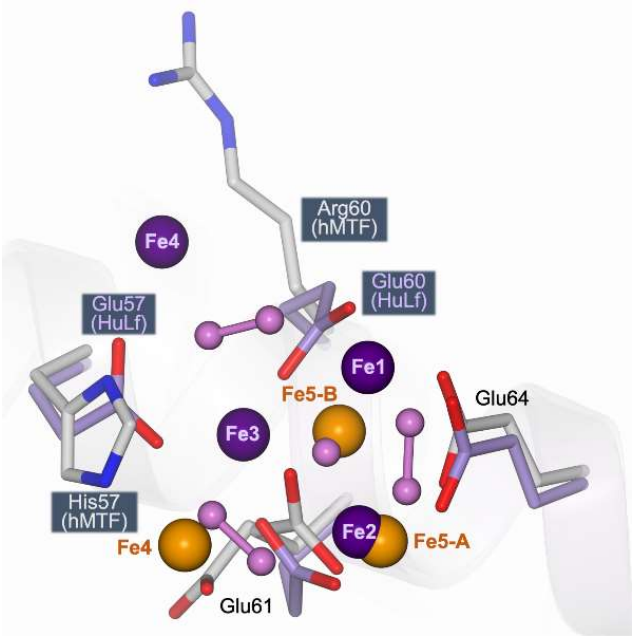

Figure 13. Structural comparison between the position occupied by the Fe5-A and Fe5-B sites identified in hMTF (light grey cartoon and carbon atoms, iron ions as orange spheres) and those of the iron ions forming the oxo-centered tri-iron(III) cluster of the nucleation site of HuLf (lilac cartoon and carbon atoms, iron ions as purple spheres, oxo and peroxide anions as pink ball-and-stick models). The position of the Fe5-A and Fe5-B sites in hMTF partially overlaps that of the oxo-centered tri-iron(III) cluster in HuLf, showing the Fe5-A ion of the former matching the position of Fe2 in the cluster. At variance with HuLf, where the cluster is fully formed (full occupancy for Fe1-Fe3 ions), the population of the mutually exclusive Fe5-A and Fe5-B sites in hMTF is only partial ranging from 25 % to 40 % (Table S1).

Conclusion

The arrangement of the iron sites as detected in the crystal structures of hMTF and the progressive population of transient iron binding sites confirm the existence of a multistep iron pathway from the inner end of the iron entry channels, corresponding to the three-fold axes pores, to the ferroxidase site, as already observed in other vertebrate ferritins.[4–6,10] Ferrous hexa-aqua ions entering the cavity are initially guided towards the negatively charged region preceding the ferroxidase site thanks to the electrostatic attraction exerted by the carboxylate residues at the bottom of the channel, on the internal protein surface.[20] The transit of Fe^{2+} species towards the ferroxidase site is assisted by conformational changes in the side chains of the residues engaged as accessory-ligands.[10] Kinetic measurements in solution at variable iron loads indicate that the catalytic iron oxidation reaction occurs via a diferric peroxo intermediate followed by the formation of ferric-oxo species. The overall iron uptake mechanism has therefore strong analogies with that observed for HuHf and *Rc*H'f, although the differences in some residues induce a slight modulation of the reaction kinetics and iron path in the proximity of the FS.[10,12,13,28] The peculiar localization of hMTF in organelles where iron trafficking and production of reactive oxygen species is intense, suggests a protective role for this enzyme against reactive oxygen species.[29] The observation of superoxide/peroxo-bound form in our structures might support such radical-scavenging role.

Experimental Section

Protein expression and purification. The gene encoding human mitochondrial ferritin (hMTF, amino acid residues 61-242), depleted of the signal sequence for mitochondrial delivery,[30] was subcloned into a pET-3a vector (GenScript, NJ, USA). Analogously to a method developed for the human heavy chain ferritin (HuHf),[4,31] the expression of hMTF was conducted in BL21(DE3)-pLys *E. coli* cells, grown in LB broth at 37 °C, and induced with 1 mM isopropyl-β-D-thiogalactoside (IPTG) when OD_{600nm} reached 0.6 – 0.8. After 4-hour incubation at 37 °C, cells were harvested and disrupted with sonication. The lysate was clarified heating at 65 °C for 15 minutes and hMTF recovered in the supernatant by ultracentrifugation. The purification process comprehended two chromatographic steps: i) anionic exchange by Q-Sepharose Fast-Flow resin (elution in 20 mM Tris pH 7.5 buffer with a 0-1 M NaCl gradient) and ii) size exclusion with a HiLoad 16 600 Superdex 200 column (GE Healthcare) in 20 mM Tris pH 7.5. Ferritin-containing fractions were identified by SDS-PAGE analysis and subjected to demineralization by extensive dialysis in the presence of reducing and chelating agents, thioglycolic acid and EDTA respectively. Protein concentration was determined using the Bradford assay or measuring the absorbance at 280 nm according to the molar extinction coefficient calculated by ProtParam tool (ε_{hMTF} 19035 M^{-1} cm^{-1} which is equal to ε_{HuHf}).

Mass spectrometry of human mitochondrial ferritin. The ESI mass spectrum of the native iron-depleted mitochondrial ferritin was performed in accordance with a well-established protocol using an AB SCIEX TripleTOF 5600$^+$ high-resolution mass spectrometer.[32–34] In detail, an aliquot of a stock solution of hMTF in ammonium acetate solution (20 mM, pH 6.8) was diluted with water (LC-MS grade) to a final protein concentration of 10^{-6} M. 0.1% of formic acid was added to the solution just before the ESI-MS analysis. The high-resolution ESI mass spectrum was acquired in positive polarity through a direct infusion at 7 μL x min^{-1} flow rate in the mass spectrometer. The ESI source parameters were: ionspray voltage floating 5500 V, ion source gas 1 (GS1) 40; ion source gas 2 (GS2) 0; curtain gas (CUR) 30, declustering potential (DP) 200 V, collision energy (CE) 10 V. For the acquisition, Analyst TF software 1.7.1 (Sciex) was used and the deconvoluted spectra were obtained by using the Bio Tool Kit micro-application v.2.2 embedded in PeakView™ software v.2.2 (Sciex).

Stopped-flow kinetic measurements. The formation of diferric peroxo (DFP) and diferric oxo/hydroxo [DFO(H)] species after the addition of an increasing amount of Fe^{2+} ions per subunit (1, 2, 4, 8 and 16; i.e. from 100 μM to 1.6 mM final iron concentration) to hMTF and HuHf was followed by the change in Abs_{650nm} and Abs_{350nm}, respectively, during the first 5 seconds (4000 data points were collected). In a UV–visible stopped-flow spectrophotometer (SX.18MV stopped-flow reaction analyzer, Applied Photophysics), 100 μM protein subunits (4.16 μM protein cages) in 200 mM 3-(N-morpholino)propanesulfonic acid (MOPS), 200 mM NaCl pH 7.0 buffer, were rapidly mixed with equal volumes of freshly prepared solutions of ferrous sulfate in 1 mM HCl.

The initial formation rates of DFP and DFO(H) species were calculated from the linear fitting of the change in absorbance at 650 and 350 nm, respectively, between 0.01–0.03 seconds. The rates referring to the decay of DFP species at 650 nm were fitted with a monoexponential function.[35] The biomineralization process was studied measuring the absorbance at 350 nm over 1000 s (100 μM protein subunits and 16 ferrous ions per subunit). All the kinetic measurements were acquired at room temperature.

Crystallization of hMTF. Crystals of hMTF were grown using the hanging-drop vapor-diffusion method at 8 °C.[36] Purified hMTF was concentrated to 20 mg mL^{-1} in 20 mM Tris-HCl pH 7.5 and stored at 4 °C until required. Drops were prepared by mixing equal volumes of protein and precipitant (1.6 – 2 M $MgCl_2$ • 6 H_2O in 0.1 M bicine pH 9) solutions and equilibrated over a 600 μL reservoir. Octahedral crystals appeared in 1 – 4 days and grew to final dimensions of 400 – 800 μm within one week. The time-controlled iron-loading study on hMTF crystals was performed under aerobic conditions by adding 1 μL of a freshly prepared saturated ammonium iron(II) sulfate (Mohr's salt, $(NH_4)_2Fe(SO_4)_2$ • 6 H_2O) solution into the crystallization drop containing preformed protein crystals.[10] Iron loading was subsequently stopped after the controlled times of 1, 3, 5, 15, 60, 90, 120 minutes by flash-freezing hMTF crystals directly in liquid nitrogen. Crystallization of hMTF was also performed under strict anaerobic conditions using the same procedure formerly reported for HuHf and *Rc*H'f.[4,10] Iron loading was performed under anaerobic conditions by flash-freezing crystals in liquid nitrogen after 3, 5, and 15 minutes of Fe(II)-exposure.

Data collection, structure solution and refinement. X-ray crystallographic data were collected using synchrotron radiation at the Diamond Light Source (DLS, Didcot, UK) beamline I03 and I04, equipped with Dectris Pilatus3 6M and Pilatus 6M-F detector, respectively (Table S4). Data were integrated using XDS,[37] and scaled with Scala,[38] from the CCP4 suite[39,40]. hMTF crystals belonged to the cubic space group F432, with the unit cell parameter *a* ~ 184 Å, varying slightly among the different crystals. Data collection and processing statistics are shown in Table S4.

Starting models were obtained by molecular replacement technique as implemented in the software Molrep,[41] using one subunit of the native enzyme (PDB id 1R03,[9] excluding non-protein atoms and solvent molecules) as searching model. Structures were refined using Refmac5,[42] from the CCP4 suite, and a protocol relying on iterative manual rebuilding through the molecular graphic software Coot,[43,44] and maximum-likelihood refinement. Water molecules were added automatically using ARP/wARP.[45] To provide unambiguous proof that we are observing iron ions full three-wavelength anomalous data were collected on the same crystal at remote high energy, peak of the Fe *K*-edge and immediately below the Fe K-edge (specific wavelength used for data collections are reported in Table S4). The positions of metal ions were determined from the anomalous Fourier difference maps calculated through *FF*T from the CCP4 suite. The anomalous signals corresponding to iron ions ranged from 4 to 55 σ in the anomalous difference maps computed from data collected at the peak of the Fe *K*-edge (Tables S1-3). The criterion applied to estimated metal ion occupancy was based on keeping atomic displacement parameters closed to those of surrounding protein atoms in fully occupied sites (water molecules bound to metal ions were refined using the same occupancy). Final models were inspected manually and checked with Coot and Procheck.[46] Structure solutions and refinement statistics are displayed in Table S5. Figures were generated using the molecular graphic software CCP4mg.[47]

Final coordinates and structure factors were deposited in the Protein Data Bank (PDB) under the accession codes 7O63 (hMTF), 7O64 (hMTF – Fe^{2+} 1 min), 7OWY (hMTF – Fe^{2+} 3 min), 7O69 (hMTF – Fe^{2+} 5 min), 7O67 (hMTF – Fe^{2+} 15 min), 7O66 (hMTF – Fe^{2+} 60 min), 7O65 (hMTF – Fe^{2+} 90 min), and 7O68 (hMTF – Fe^{2+} 120 min), 7O6D (hMTF – Fe^{2+} 3 min, anaerobic environment), 7O6A (hMTF – Fe^{2+} 5 min, anaerobic environment), 7O6C (hMTF – Fe^{2+} 15 min, anaerobic environment).

Acknowledgements

We acknowledge the synchrotron facility Diamond Light Source for providing us beamtime and thank the Diamond staff, in particular people working on beamlines I03 and I04 for their assistance during the experimental sessions. The research leading to this result has been supported by the project CALIPSOplus under the Grant Agreement 730872 from the EU Framework Programme for Research and Innovation HORIZON 2020. The authors acknowledge the use of resources of Instruct-ERIC, a Landmark ESFRI project, and specifically the CERM/CIRMMP Italy Centre and AIRC for funding the project "Advanced Mass Spectrometry Tools for Cancer Research: Novel Applications in Proteomics, Metabolomics and Nanomedicine" (Multiuser Equipment Program 2016, ref. code 19650). The financial support provided by the MIUR Grant Dipartimento di Eccellenza 2018-2022 to both the Department of Biotechnology, Chemistry and Pharmacy of the University of Siena and the Department of Chemistry "Ugo Schiff" of the University of Florence is also acknowledged.

Keywords: human mitochondrial ferritin • ferroxidase site • ferroxidase reaction • accessory transient sites

[1] E. C. Theil, R. K. Behera, T. Tosha, *Coord Chem Rev* **2013**, *257*, 579–586.
[2] A. Cozzi, B. Corsi, S. Levi, P. Santambrogio, G. Biasiotto, P. Arosio, *Blood* **2004**, *103*, 2377–2383.
[3] Y. H. Wang, S. R. Sczekan, E. C. Theil, *Nucleic Acids Res* **1990**, *18*, 4463–4468.
[4] C. Pozzi, F. Di Pisa, C. Bernacchioni, S. Ciambellotti, P. Turano, S. Mangani, *Acta Crystallogr. D Biol. Crystallogr.* **2015**, *71*, 1909–1920.
[5] C. Pozzi, S. Ciambellotti, C. Bernacchioni, F. Di Pisa, S. Mangani, P. Turano, *Proc. Natl. Acad. Sci. U.S.A.* **2017**, *114*, 2580–2585.
[6] S. Ciambellotti, C. Pozzi, S. Mangani, P. Turano, *Chemistry – A European Journal* **2020**, *26*, 5770–5773.
[7] S. Levi, B. Corsi, M. Bosisio, R. Invernizzi, A. Volz, D. Sanford, P. Arosio, J. Drysdale, *J. Biol. Chem.* **2001**, *276*, 24437–24440.
[8] B. Corsi, A. Cozzi, P. Arosio, J. Drysdale, P. Santambrogio, A. Campanella, G. Biasiotto, A. Albertini, S. Levi, *J Biol Chem* **2002**, *277*, 22430–22437.
[9] B. Langlois d'Estaintot, P. Santambrogio, T. Granier, B. Gallois, J. M. Chevalier, G. Précigoux, S. Levi, P. Arosio, *J. Mol. Biol.* **2004**, *340*, 277–293.
[10] C. Pozzi, F. Di Pisa, D. Lalli, C. Rosa, E. Theil, P. Turano, S. Mangani, *Acta Crystallogr. D Biol. Crystallogr.* **2015**, *71*, 941–953.
[11] R. L. Levine, L. Mosoni, B. S. Berlett, E. R. Stadtman, *PNAS* **1996**, *93*, 15036–15040.
[12] C. Bernacchioni, C. Pozzi, F. Di Pisa, S. Mangani, P. Turano, *Chemistry* **2016**, *22*, 16213–16219.
[13] C. Pozzi, F. Di Pisa, D. Lalli, C. Rosa, P. Turano, S. Mangani, *J Inorg Biochem* **2019**, *197*, 110697.
[14] S. Hong, K. D. Sutherlin, J. Park, E. Kwon, M. A. Siegler, E. I. Solomon, W. Nam, *Nat Commun* **2014**, *5*, 5440.
[15] D. A. Whittington, S. J. Lippard, *J. Am. Chem. Soc.* **2001**, *123*, 827–838.
[16] S. H. Kim, G. Xing, Bollinger J. Martin, C. Krebs, B. M. Hoffman, *J. Am. Chem. Soc.* **2006**, *128*, 10374–10375.
[17] E. C. Theil, P. Turano, V. Ghini, M. Allegrozzi, C. Bernacchioni, *J Biol Inorg Chem* **2014**, *19*, 615–622.
[18] C. Bernacchioni, V. Ghini, E. C. Theil, P. Turano, *RSC Adv.* **2016**, *6*, 21219–21227.
[19] B. Chandramouli, C. Bernacchioni, D. Di Maio, P. Turano, G. Brancato, *J. Biol. Chem.* **2016**, *291*, 25617–25628.
[20] R. K. Behera, E. C. Theil, *PNAS* **2014**, *111*, 7925–7930.
[21] S. Haldar, L. E. Bevers, T. Tosha, E. C. Theil, *J Biol Chem* **2011**, *286*, 25620–25627.
[22] F. Bou-Abdallah, P. Santambrogio, S. Levi, P. Arosio, N. D. Chasteen, *J. Mol. Biol.* **2005**, *347*, 543–554.
[23] A. Majumdar, U.-P. Apfel, Y. Jiang, P. Moënne-Loccoz, S. J. Lippard, *Inorg Chem* **2014**, *53*, 167–181.
[24] E. Y. Tshuva, S. J. Lippard, *Chem Rev* **2004**, *104*, 987–1012.
[25] T. Ookubo, H. Sugimoto, T. Nagayama, H. Masuda, T. Sato, K. Tanaka, Y. Maeda, H. Ōkawa, Y. Hayashi, A. Uehara, M. Suzuki, *J. Am. Chem. Soc.* **1996**, *118*, 701–702.
[26] J. M. Bradley, D. A. Svistunenko, J. Pullin, N. Hill, R. K. Stuart, B. Palenik, M. T. Wilson, A. M. Hemmings, G. R. Moore, N. E. Le Brun, *Proc Natl Acad Sci U S A* **2019**, *116*, 2058–2067.
[27] T. Masuda, F. Goto, T. Yoshihara, B. Mikami, *Biochem Biophys Res Commun* **2010**, *400*, 94–99.
[28] C. Bernacchioni, S. Ciambellotti, E. C. Theil, P. Turano, *Biochim. Biophys. Acta* **2015**, *1854*, 1118–1122.
[29] S. Levi, P. Arosio, *Int J Biochem Cell Biol* **2004**, *36*, 1887–1889.
[30] J. Drysdale, P. Arosio, R. Invernizzi, M. Cazzola, A. Volz, B. Corsi, G. Biasiotto, S. Levi, *Blood Cells Mol. Dis.* **2002**, *29*, 376–383.
[31] E. Ravera, S. Ciambellotti, L. Cerofolini, T. Martelli, T. Kozyreva, C. Bernacchioni, S. Giuntini, M. Fragai, P. Turano, C. Luchinat, *Angew. Chem. Int. Ed. Engl.* **2016**, *55*, 2446–2449.
[32] A. Pratesi, D. Cirri, L. Ciofi, L. Messori, *Inorg Chem* **2018**, *57*, 10507–10510.
[33] E. Michelucci, G. Pieraccini, G. Moneti, C. Gabbiani, A. Pratesi, L. Messori, *Talanta* **2017**, *167*, 30–38.
[34] L. Biancalana, A. Pratesi, F. Chiellini, S. Zacchini, T. Funaioli, C. Gabbiani, F. Marchetti, *New J. Chem.* **2017**, *41*, 14574–14588.
[35] T. Tosha, R. K. Behera, E. C. Theil, *Inorg Chem* **2012**, *51*, 11406–11411.
[36] M. Benvenuti, S. Mangani, *Nat Protoc* **2007**, *2*, 1633–1651.
[37] W. Kabsch, *Acta Crystallogr D Biol Crystallogr* **2010**, *66*, 125–132.
[38] P. Evans, *Acta Crystallogr D Biol Crystallogr* **2006**, *62*, 72–82.
[39] M. D. Winn, C. C. Ballard, K. D. Cowtan, E. J. Dodson, P. Emsley, P. R. Evans, R. M. Keegan, E. B. Krissinel, A. G. W. Leslie, A. McCoy, S. J. McNicholas, G. N. Murshudov, N. S. Pannu, E. A. Potterton, H. R. Powell, R. J. Read, A. Vagin, K. S. Wilson, *Acta Crystallogr D Biol Crystallogr* **2011**, *67*, 235–242.
[40] Collaborative Computational Project, Number 4, *Acta Crystallogr D Biol Crystallogr* **1994**, *50*, 760–763.
[41] A. Vagin, A. Teplyakov, *Acta Crystallogr D Biol Crystallogr* **2010**, *66*, 22–25.
[42] G. N. Murshudov, P. Skubák, A. A. Lebedev, N. S. Pannu, R. A. Steiner, R. A. Nicholls, M. D. Winn, F. Long, A. A. Vagin, *Acta Crystallogr D Biol Crystallogr* **2011**, *67*, 355–367.
[43] P. Emsley, K. Cowtan, *Acta Crystallogr D Biol Crystallogr* **2004**, *60*, 2126–2132.
[44] P. Emsley, B. Lohkamp, W. G. Scott, K. Cowtan, *Acta Crystallogr D Biol Crystallogr* **2010**, *66*, 486–501.
[45] G. Langer, S. X. Cohen, V. S. Lamzin, A. Perrakis, *Nat Protoc* **2008**, *3*, 1171–1179.
[46] R. A. Laskowski, M. W. MacArthur, J. M. Thornton, *Curr Opin Struct Biol* **1998**, *8*, 631–639.
[47] S. McNicholas, E. Potterton, K. S. Wilson, M. E. M. Noble, *Acta Crystallogr. D Biol. Crystallogr.* **2011**, *67*, 386–394.